

Weierstraß-Institut für Angewandte Analysis und Stochastik

im Forschungsverbund Berlin e. V.

Preprint

ISSN 0946 – 8633

Impact of slippage on the morphology and stability of a dewetting rim

Andreas Münch¹, Barbara Wagner²

submitted: October 29, 2010

¹ Mathematical Institute,
24-29 St Giles',
University of Oxford,
Oxford, OX1 3LB, UK

² Weierstrass Institute for Applied Analysis and Stochastics,
Mohrenstraße 39,
10117 Berlin, Germany

No. 1556
Berlin 2010



2000 *Mathematics Subject Classification.* 34E15, 35B36, 76D08.

Key words and phrases. asymptotic expansions, dewetting films, stability analysis.

Edited by

Weierstraß-Institut für Angewandte Analysis und Stochastik (WIAS)
Mohrenstraße 39
10117 Berlin
Germany

Fax: +49 30 2044975

E-Mail: preprint@wias-berlin.de

World Wide Web: <http://www.wias-berlin.de/>

Abstract

In this study lubrication theory is used to describe the stability and morphology of the rim that forms as a thin polymer film dewets from a hydrophobized silicon wafer. Thin film equations are derived from the governing hydrodynamic equations for the polymer to enable the systematic mathematical and numerical analysis of the properties of the solutions for different regimes of slippage and for a range of time scales.

Dewetting rates and the cross sectional profiles of the evolving rims are derived for these models and compared to experimental results. Experiments also show that the rim is typically unstable in the spanwise direction and develops thicker and thinner parts that may grow into “fingers”. Linear stability analysis as well as nonlinear numerical solutions are presented to investigate shape and growth rate of the rim instability. It is demonstrated that the difference in morphology and the rate at which the instability develops can be directly attributed to the magnitude of slippage. Finally, a derivation is given for the dominant wavelength of the bulges along the unstable rim.

1 Introduction

Rim instabilities for thin liquid films that wet a solid substrate have been studied for decades, both theoretically and experimentally [1, 2, 3, 4, 5, 6, 7, 8]. The mathematical models typically exploit the large separation of length scales to obtain a simplified thin film equations from the underlying Navier-Stokes equations in conjunction with conservation of mass. For most wetting scenarios the type of boundary condition at the liquid/solid interface typically enters only weakly and does not influence the morphology or stability properties of the film, see for example [3, 7, 9, 10].

The picture is different when the thickness of the liquid is only on the scale of a few hundred nanometers and placed on a hydrophobically coated substrate. This is the situation for polymer films that dewet after they have been heated above the glass transition temperature. This is the situation for experiments carried out by a number groups [11, 12, 13, 14, 15] to name but a few. The dewetting begins after the deposited polymer films are heated above the glass transition temperature and holes have formed, either spontaneously, through spinodal decomposition, or by nucleation. The dewetting i.e. hole growth is driven by van-der-Waals forces that make it energetically favourable to decrease the area of the substrate covered by the originally deposited polymer film.

In the beginning of the dewetting process, holes are formed that grow; the receding liquid accumulates in a capillary rim at the perimeter of the hole. This rim increases in width and height as the dewetting proceeds. While in some experiments the growth of the hole continues until it collides with neighboring holes and then the remaining ridges destabilize into droplets via a Rayleigh-Plateau instability [16, 17], in others the rim of the hole destabilizes while it grows and gives rise to finger-like structures that eventually pinch-off and form droplets. Such finger-like instabilities have also been observed for planar as opposed to axisymmetric dewetting, see [11, 18, 19, 20, 21, 22, 23] and in other related situations [12, 13, 13, 24, 25, 26, 27, 28, 29, 30, 31].

The effect of slippage on the shape and dewetting rate was first investigated in [14, 32]. Scaling arguments were used to predict that for substantial slip at the liquid/solid interface, the position of the contact line follows a $t^{2/3}$ law in contrast to a linear behavior in the no-slip situation. The size dependence of the dewetting rate in the slip case was further explored in [33], where the authors suggest and give experimental evidence that this has a strong positive effect on promoting the fingering instability. For the early stages of rupture, the effect of different magnitudes of slip was investigated in [34].

Moreover experimental results by Fetzer et al. [15] show that there is a transition of the cross section of the rim from an oscillatory decay to a monotone decay towards the undisturbed (wet) side of the rim, simply by changing the hydrophobic coating. This was explained to be due to the difference in magnitude of the interfacial slippage of the liquid and the coating in [15, 27], followed by a quantitative comparison with theoretical predictions [35] on the basis of thin film equations derived asymptotically from the underlying Navier-Stokes equations. In addition, in [36, 37] it was shown that viscoelastic effects alone using the Jeffreys model cannot explain this morphological transition.

In order to systematically investigate the impact of slippage on the dynamics and morphology of dewetting films Fetzer et al., Bäumchen et al. [15, 35, 38, 39] and Marquant et al. [40] used, as a model system, Polystyrene (PS) below the entanglement length, dewetting from a silicon/silicon oxide wafer that has been treated with coatings of either self-assembled monolayers of Octadecyltrichlorosilane (OTS) or Dodecyltrichlorosilane (DTS) or of spin coated amorphous AF 1600 Teflon. Both hole and planar (trench) dewetting were investigated.

In this paper we present our theory for these nano- and microfluidic phenomena on the basis of the presence of interfacial slippage. Building on our past work we aim here to present a comprehensive picture in form of a continuum theory that connects the experimental observations and relates them to the dominant physical forces that interact on these scales. In particular, we summarize our previous results on the shape of the cross sections of the evolving rims and expand our mathematical approach to the “finger” instability to give an estimate of the dominant wavelength.

2 Mathematical models

The dewetting process described in the introduction represents a slow laminar flow of a very viscous polymer. The polymer is assumed to be below the entanglement length allowing us to assume that elastic effects do not play a role. The governing equations describing this dewetting process are given by the Navier-Stokes equations for viscous incompressible flow of a fluid layer on $0 \leq Z \leq H(X, Y, T)$ with

$$\rho(\partial_T \mathbf{U} + \mathbf{U} \cdot \nabla \mathbf{U}) = -\nabla(P + F'(H)) + \mu \nabla^2 \mathbf{U}, \quad (2.1)$$

$$\nabla \cdot \mathbf{U} = 0. \quad (2.2)$$

Here, $\mathbf{U} = (U(X, Y, Z, T), V(X, Y, Z, T), W(X, Y, Z, T))$ denotes the velocity field, $P = P(X, Y, Z, T)$ the pressure field, ρ the density, μ the viscosity and $F'(H) = dF/dH$ the contribution due to an intermolecular potential $F(H)$.

The boundary conditions at the free surface $Z = H(X, Y, T)$, are given by the kinematic condition

$$\partial_T H = -\nabla_{XY} \cdot \int_0^H \mathbf{U}_{XY} dZ, \quad (2.3)$$

and the normal and tangential stress conditions

$$\mathbf{n} \cdot (\boldsymbol{\tau} - P \mathbf{I}) \cdot \mathbf{n} = 2\sigma\kappa, \quad \mathbf{t} \cdot (\boldsymbol{\tau} - P \mathbf{I}) \cdot \mathbf{n} = 0, \quad (2.4)$$

with constant surface tension σ , respectively. We denote $\nabla_{XY} = (\partial_X, \partial_Y)$, $\mathbf{U}_{XY} = (U, V)$ and define the normal and tangential vectors by

$$\mathbf{n} = \frac{(-\nabla_{XY} H, 1)}{(1 + (\nabla_{XY} H)^2)^{1/2}} \quad \text{and} \quad \mathbf{t} = \frac{1}{((\nabla_{XY} H)^2 [1 + (\nabla_{XY} H)^2])^{1/2}} \begin{pmatrix} \nabla_{XY} H \\ (\nabla_{XY} H)^2 \end{pmatrix} \quad (2.5)$$

The local mean curvature is then given by $\kappa = \nabla_{XY} \cdot \mathbf{n}$. In a Newtonian flow $\boldsymbol{\tau}$ is proportional to the strain rate, i.e. $\boldsymbol{\tau} = \mu \dot{\gamma}$, where $\dot{\gamma}_{ij} = \partial_i U_j + \partial_j U_i$.

The driving forces of the dewetting are intermolecular forces and is described by an effective interface potential, that consists of long-range attractive van der Waals contributions and a short range Born repulsion term that penalizes the thinning of the film below a minimum threshold H^* . The experimental situation as given in [41, 42], where a silicon wafer, that is coated with a native SiO layer of thickness d_{SiO} , which is coated by another hydrophobic layer of DTS, OTS or AF 1600 Teflon of thickness d_c , leads to the potential [41]

$$F(H) = \frac{C_c}{H^8} - \frac{A_c}{12\pi H^2} + \frac{A_c - A_{\text{SiO}}}{12\pi(H + d_c)^2} + \frac{A_{\text{SiO}} - A_{\text{Si}}}{12\pi(H + d_c + d_{\text{SiO}})^2} \quad (2.6)$$

The constant C_c denotes the strength of the short range repulsion and $A_{\text{Si}}, A_{\text{SiO}}, A_c$ denote the Hamaker constants of polystyrene with the different substrate layers, Si, SiO and the hydrophobic coating, respectively.

It turns that for dewetting scenarios discussed here, the last two terms can be neglected with little or no change to the numerical and asymptotic results. Therefore, we will mostly use the simpler two-term potential

$$F(H) = \frac{C_c}{H^8} - \frac{A_c}{12\pi H^2}, \quad (2.7)$$

and occasionally the three-term variant

$$F(H) = \frac{C_c}{H^8} - \frac{A_c}{12\pi H^2} + \frac{A_{\text{SiO}} - A_{\text{Si}}}{12\pi(H + d_c + d_{\text{SiO}})^2} \quad (2.8)$$

where the third term has been dropped since in the experiments we consider here $A_c \approx A_{\text{SiO}}$.

For the boundary conditions at the solid surface at $Z = 0$ we require impermeability. The central assumption on the non-Newtonian behaviour or complex nature of the dewetting polymer, is essentially contained in a thin layer between the polymer film and the substrate, that is hydrophobically coated with a self-assembled monolayer, here OTS and DTS. Specifically, it is argued in [43] and extended further in [44], that due to a coil-stretch transition of the chains of a self-assembled monolayer, an unusually high slippage may be expected due to the resulting decrease of viscosity there. In our continuum formulation we approximate this by an effective slip boundary condition, the Navier slip condition

$$U = B \partial_Z U, \quad (2.9)$$

and investigate the changes in the solution, their morphology and stability properties, as the slip length parameter B varies by several orders of magnitude.

We nondimensionalize the problem by introducing the scales

$$\begin{aligned} Z &= \mathbb{H}z, & X &= \mathbb{L}x, & Y &= \mathbb{L}y, & H &= \mathbb{H}h, & B &= \mathbb{H}b, \\ U &= \mathbb{U}u, & V &= \mathbb{U}v, & W &= \mathbb{W}w, & T &= \frac{\mathbb{H}}{\mathbb{W}}t, & P + F' &= \mathbb{P}p, \\ F' &= \mathbb{P}\phi'. \end{aligned} \quad (2.10)$$

and note that for the thin film flows such as considered here it is typically of great advantage to use the fact that the ratio of the characteristic length scales in the vertical and lateral directions of the evolving film profiles is small, i.e. we assume $\varepsilon_{lub} = \mathbb{L}/\mathbb{H} \ll 1$. This simplifies the governing equations so that the remaining problems can be integrated with respect to Z to obtain dimension-reduced thin film equations for the profile $H(X, Y, T)$.

In fact, a family of closed form thin film equations was derived in the asymptotic limit of small ε_{lub} for various orders of magnitude of the slip length [27]. Two distinguished limits were established. They essentially go back to the different balances in the governing equations that are required for the flow fields corresponding to the order of magnitude of the slip length. For small slip lengths the flow field has a parabolic profile (see figure 1, left) and the horizontal pressure gradients balances the most dominant

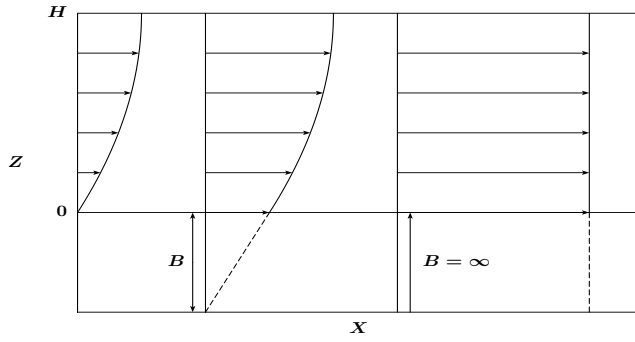


Figure 1: Sketch of flow profiles for increasing slippage.

viscous contribution, while for very large slip length the constant flow field typical for plug flow (see figure 1, right) requires the balance of the vertical pressure gradient with the dominant viscous term. The distinguished limits are

the *weak-slip regime*:

$$\partial_t h = -\nabla \cdot [(h^3 + bh^2) \nabla \cdot (\Delta h - \phi'(h))]. \quad (2.11)$$

with the limiting case $b = 0$; i.e. the well-known no-slip lubrication equation.

The *strong-slip regime*, a coupled system of equations for the horizontal velocities $u(x, y, t)$, $v(x, y, t)$ and the film profile $h(x, y, t)$

$$\text{Re} \frac{du}{dt} = \frac{1}{h} [\partial_x (4h\partial_x u + 2h\partial_y v) + \partial_y (h\partial_x v + h\partial_y u)] + \partial_x [\Delta h + \phi'(h)] - \frac{u}{h\beta}, \quad (2.12)$$

$$\text{Re} \frac{dv}{dt} = \frac{1}{h} [\partial_y (4h\partial_y v + 2h\partial_x u) + \partial_x (h\partial_x v + h\partial_y u)] + \partial_y [\Delta h + \phi'(h)] - \frac{v}{h\beta}, \quad (2.13)$$

$$\partial_t h = -\partial_x (h u) - \partial_y (h v), \quad (2.14)$$

where we denote the total derivative by $d/dt = \partial_t + u \partial_x + v \partial_y$, the Laplace operator by $\Delta = \partial_x^2 + \partial_y^2$ and $\text{Re} = \rho U L / \mu$ is the Reynolds number. For this model the slip length is large and of order $b = \beta/\varepsilon_{lub}^2$. By choosing

Both models use the non-dimensionalized form of the two-term intermolecular potential (2.7),

$$\phi(h) = \frac{1}{8(h/\varepsilon)^8} - \frac{1}{2(h/\varepsilon)^2}, \quad (2.15)$$

or of the three-term potential (2.8),

$$\Phi(h) = \frac{a_1}{8(h/\varepsilon)^8} - \frac{a_2}{2(h/\varepsilon)^2} + \frac{a_3}{((h/\varepsilon) + d)^3}, \quad (2.16)$$

with

$$a_1 = 1.014, \quad a_2 = 1.014, \quad a_3 = 7.465 \quad \text{and} \quad d = 25.34,$$

where $\varepsilon = H_{\min}/H$, and H_{\min} is the thickness where each of the dimensional potentials (2.7) or (2.8) achieves its minimum value.

In [27] a detailed derivation of these thin film models is given in two dimensions. The generalization to three dimensions, presented here is a rather straight forward extension of that analysis.

The *strong-slip regime* and the *weak-slip regime* have as the limiting case a regime, where the slip-length is intermediate to both of them

$$\partial_t h = -\nabla \cdot [h^2 \nabla \cdot (\Delta h - \phi'(h))] \quad (2.17)$$

and called the *intermediate-slip regime*. This regime is obtained for slip lengths $b = O(\beta/\varepsilon_{lub})$.

We note that for the highly viscous flows considered here, the Reynolds number is extremely small and inertial effects will be neglected in the rest of the paper.

3 Cross sections of rims

Shortly after the dewetting has begun, liquid polymer will accumulate near the dewetting front and leads eventually to the formation of a rim that merges into the undisturbed film leaving behind a film of minimal thickness H^* . This rim typically attains a specific shape before it undergoes a Rayleigh-Plateau type instability along the dewetting front. We will next give an overview of the possible cross sectional shapes for the various regimes and demonstrate that the cross sectional shape of the rim directly depends on and quantitatively reflects the size of the slip length. Recent experimental results on the long-time profiles of the cross section of the rims for different hydrophobic coatings are shown for comparison.

3.1 No-slip case

Most well-known is the no-slip case. The evolution of the liquid film profile is given by the one-dimensional version of (2.11) with $b = 0$,

$$\partial_t h = -\partial_x [h^3 \partial_x (\partial_{xx} h - \varepsilon^{-1} \Phi'(h/\varepsilon))], \quad (3.1)$$

where we use the normalized potential $\Phi(h/\varepsilon) = \phi(h)$ and $\varepsilon = H^*/H$, together with the far-field conditions

$$\lim_{x \rightarrow -\infty} h(x, t) = \varepsilon \quad \text{and} \quad \lim_{x \rightarrow \infty} h(x, t) = 1. \quad (3.2)$$

Let us denote by $s(t)$ the position of the dewetting front towards the dewetted side and by $s(t) + w(t)$ the position of the front merging into the undisturbed film, i.e. $w(t)$ denotes the width of the growing rim, see the figure 2.

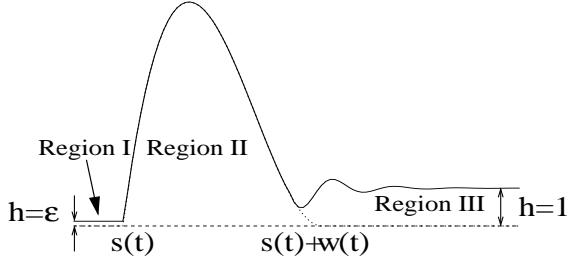


Figure 2: Sketch of rim profile.

As is well-known, without slip the dewetting velocity depends singularly on the residual film thickness ε , i.e. if $x = s(t)$ denotes the position of the dewetting front then $\dot{s} \sim 1/\ln(1/\varepsilon) \rightarrow 0$ as $\varepsilon \rightarrow 0$, see e.g. [45]. The detailed matched asymptotic argument by Flitton and King [45], extended by Münch et al. [27] to take into account the effective interface potential, show that in the latter case, by matching the regions I to III to region II in figure 2, the following asymptotic formula for the position can be derived

$$s(t) \sim \bar{\delta}t \frac{(\tan \theta)^3}{3(\bar{\delta} \log t + 1)}, \quad \text{where } \bar{\delta} = 1/\ln(1/\varepsilon) \quad (3.3)$$

and θ is the contact angle, defined by $\tan(\theta) = \sqrt{-2\Phi(1)}$, where $\Phi(1) < 0$. The leading order solution for the rim profiles has the parabolic form [45],

$$h(x, t) = \frac{6s(t)}{w(t)^3} (x - s(t))(s(t) + w(t) - x), \quad (3.4)$$

where the width of the rim satisfies

$$w(t) \sim \bar{\delta}^{1/2} t^{1/2} \frac{2^{2/3} \tan \theta}{(\bar{\delta} \log t)^{1/6} (1 + \bar{\delta} \log t)^{1/3}} \quad (3.5)$$

and the slope of the profile at the dewetting front as $t \rightarrow \infty$, the slope of the profile is

$$\partial_x h(s(t), t) = \frac{6s}{w^2} = 2^{1/3} \frac{(\bar{\delta} \log t)^{1/3}}{1 + (\bar{\delta} \log t)^{1/3}} \tan \theta.$$

i.e. it asymptotes to a value that is $2^{1/3}$ times the slope of a static contact angle.

3.2 Intermediate-slip case

For the intermediate-slip case the problem for the cross-sectional profile reads

$$\partial_t h = -\partial_x \left[h^2 \partial_x (\partial_{xx} h - \varepsilon^{-1} \Phi'(h/\varepsilon)) \right], \quad (3.6)$$

together with boundary conditions

$$\lim_{x \rightarrow -\infty} h(x, y, t) = \varepsilon \quad \text{and} \quad \lim_{x \rightarrow \infty} h(x, y, t) = 1. \quad (3.7)$$

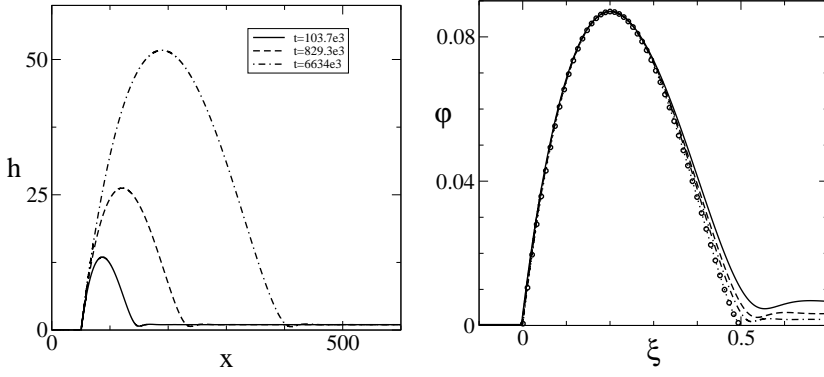


Figure 3: (a) Evolution of the dewetting rim profile obtained by solving (3.6), (3.7), with the intermolecular potential (2.16) and $\epsilon = 0.04$. (b) The same rim profiles rescaled as explained in the text, using the same line styles as on the left. The fourth profile, shown by open circles, corresponds to the solutions φ of (3.9), (3.10).

As for the no-slip case a matched asymptotic argument has been carried out to yield an expression for the position of the dewetting front, see [27]

$$s(t) = \left(\frac{3}{2}\right)^{2/3} 0.0272 (\tan \theta)^{5/3} t^{2/3}. \quad (3.8)$$

The corresponding rim shape is obtained from a matched asymptotics analysis for (3.6), (3.7), which yields the leading order outer problem [45]

$$\varphi \varphi''' = 1, \quad \text{where } ' = d/d\xi, \quad (3.9)$$

and boundary conditions

$$\begin{aligned} \varphi &= 0, & \varphi' &= 1, & \varphi^2 \varphi''' &= 0 \text{ at } \xi = 0, \\ \varphi &\sim 2(2/3)^{1/2} (d - \xi)^{3/2} & \text{as } \xi \rightarrow d. \end{aligned} \quad (3.10)$$

Here, the profile has been rescaled according to

$$h = (\lambda^3/\dot{s})\varphi, \quad x = (\lambda^2/\dot{s})\xi + s^-, \quad s^+ = (\lambda^2/\dot{s})d + s^-. \quad (3.11)$$

The problem (3.9), (3.10) has been investigated before by Boatto et al. [46] where it was found that solutions exist if $d = 1/2$. Solving the problem (3.6), (3.7) numerically for a long time we find that eventually the solutions approach a universal shape φ that is given by the solution of the asymptotic ODE problem (3.9), (3.10).

Indeed, this can be seen most clearly when the profiles are shifted to the same lateral position and rescaled to have a maximum height of one,

$$h = \frac{\max_x(h(x,t))}{\max_\xi(\varphi(\xi))} \varphi \quad x = \frac{\max_x(h(x,t))}{\lambda \max_\xi(\varphi(\xi))} \xi. \quad (3.12)$$

The lateral length scale is found from the scaling for h and (3.11). The result is shown in figure 3(b). We clearly see that the rescaled solutions of the full lubrication model converge in time to a universal shape given by the solution φ of (3.9), (3.10).

Interestingly, the results show that the rim is asymmetric with respect to the vertical axis going through the maximum of the rim. The width of the portion to the right of this axis is about $3/2$ the width of the portion to the left. Later in this section we will make comparisons of these rim shapes with long-time experiments for PS dewetting from the DTS coated silicon/silicon oxide wafer.

Another important observation is the fact that dewetting rates of the rim for the intermediate-slip regime is $\dot{s}(t) \sim t^{-1/3}$, which means that as the rim grows it will slow down. This is in contrast to the situation for no-slip and also for very large slip in the strong-slip regime, where the dewetting rate is almost constant (as explained in the previous and the following section). This property has important implications for our discussion of the rim instability further below.

3.3 Strong-slip case

The experiments by Fetzer et al. [15] on the transition in the cross sectional shape of the rim for different hydrophobic coatings, focussed on the rim shapes of PS dewetting on OTS and on DTS after their dewetting fronts have travelled the same distance and so have accumulated and transported the same volume of liquid. To ensure that the bulk material properties of PS were not altered, the temperature was kept constant. Nevertheless, the dewetting of DTS was much faster than for OTS, and while on the OTS coating the spatial decay of the rim onto the rim was oscillatory, it was monotonic on DTS. The changes in the rim profile was explained with the difference in friction between the liquid PS and the coating layer which is reflected, in our continuum formulation, by large differences in slippage. The effect of grafted brushes on the amount of slippage/friction at the interface between a solid substrate and a polymer liquid has been attributed to a coil-stretch transition [32, 44]. It is therefore plausible that the different chain lengths of the otherwise chemically identical OTS and DTS brushes could be the reason the difference of the apparent slippage inferred from the experimental observations of the cross sectional rim shape.

However, the thin film models for weak- and intermediate-slip show rim profiles that always have oscillatory decaying tails. Moreover, it was shown in [36, 37] that including viscoelasticity into the film models will not lead to rim tails having monotone decay.

The transition from an oscillatory to a monotonic profile only occurs for large enough slip-lengths, where the strong-slip model is valid; rim profiles for the intermediate and weak-slip models, profiles always show decaying oscillations. This is also true if viscoelasticity is included, i.e. profiles will have a monotonically decaying profile only if enough slippage is present [36, 37].

The transition can be observed most easily via a linear stability analysis about the undisturbed flat film $h = 1$, $u = 0$. For this purpose, we shift the lateral x coordinate

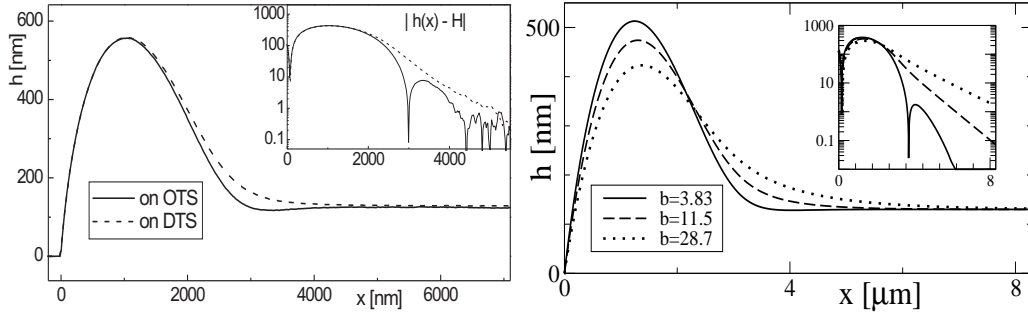


Figure 4: Left: Rim profiles of 130 nm PS films on DTS and OTS coated Si/SiO wafers at constant temperature $T = 120^\circ\text{C}$ (the inset depicts a semilog plot of $|h(x) - H|$). Profiles are shown with the dewetting front shifted into the origin. While PS on OTS show rim profiles with oscillatory decay of the rim, the rim of PS on DTS has a monotone decay.(By courtesy of Karin Jacobs, Saarland University). Right: Rim profiles for different slip lengths b non-dimensionalized with $H = 130 \text{ nm}$. The inset shows a semilog plot of $\max(|h(x) - H|, 10^{-5})$.

to the frame moving with the rim $\xi = x - s(t)$ and introduce a small ($\delta \ll 1$) normal modes perturbation of the flat state,

$$h(x, t) = 1 + \delta h_1 e^{\omega \xi}, \quad u = \delta v_1 e^{\omega \xi}. \quad (3.13)$$

The exponent ω must have negative real part to ensure spatial decay. The order $O(\delta)$ problem results in a third order polynomial equation for ω . The solutions with negative real part are complex exactly if the discriminant

$$D = 1 - \frac{4^4 \dot{s}^2}{3^3} \beta \quad (3.14)$$

is positive, thus indicating oscillatory decay in particular for small $\beta \rightarrow 0$. Increasing the slip parameter increases \dot{s} and therefore decreases D until it becomes negative so that we see a transition to a monotonic decay.

For the data supplied by the experiment in Fetzer et al. [15] the numerical solutions of the one dimensional, inertialess version of (2.12) confirms the prediction from the linear stability analysis, see figure 4.

Interestingly, the transition in the profile can also be obtained for the same hydrophobic coating by increasing the temperature and thereby reducing the viscosity, thus changing the value of \dot{s} , provided the amount of slippage is in the proper range. Moreover, we note that the above analysis can be refined by linearizing the full Stokes model instead of the thin film equation and has led to a new method for determining the slip length from experimental measurements of the profile [35].

3.4 Long-time evolution of rims

An interesting recent observation by Marquant e al. [40] was that a PS film of 130 nm thickness dewetting from a DTS coated silicon wafer eventually also develops

rim tails with oscillating decay. In this experiment the dewetting was initialized with a straight contact line. The evolution of the rim was monitored while the area of the cross section increased by several orders of magnitude (figure 5). The initially monotonic decay of the rim profile eventually develops oscillations (figure 6). Moreover, when the profiles are shifted such that they all start at the origin, scaled so that the maxima of their height is one and the horizontal scale accordingly the profiles assume a universal asymmetric shape for large time, that resembles the large-time asymptotic profile we found for the intermediate-slip regime (figure 3(b)). If the location of the maxima is scaled to 0.2 one obtains the signature of the rim shapes for the intermediate-slip regime, where the width on the right side of the maximum is 3/2 the width of the left side, shown in figure 5(right).

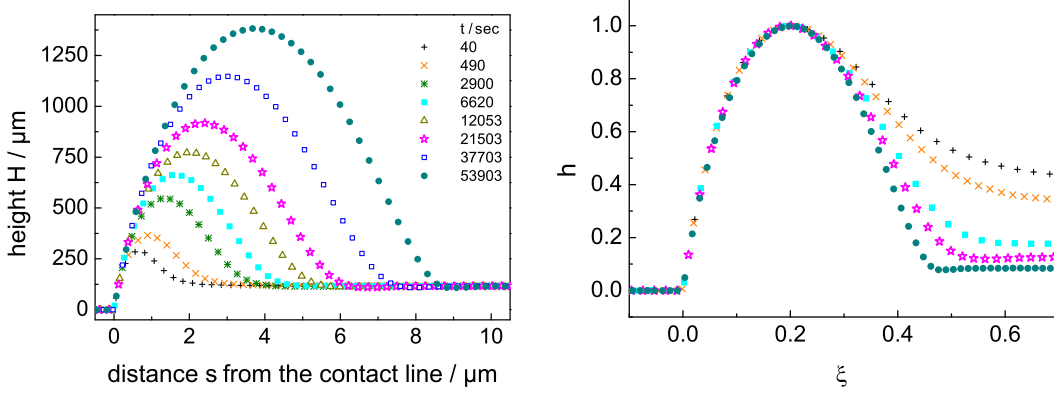


Figure 5: Left: Rim shapes of PS(10.3k) at 110°C of thickness 120(5) nm dewetting from a DTS coated Si/SiO wafer. For easy comparison all dewetting fronts are shifted to the origin. Rim shapes are monitored until the area of the rim has reached manyfold its original area at the early stages of the dewetting. The legend indicates the time (in seconds), the measurement of the rim took place. In order to distinguish the symbols for the different curves, the density of points have been reduced. Right: Normalized cross sections of the rims corresponding to $t = 40(+)$, $t = 490(\times)$, $t = 6620(\bullet)$, $t = 21503(\star)$, $t = 53903(\bullet)$ to illustrate the approach to a universal shape. The heights are all scaled to 1 and the widths accordingly. The limiting rim shape has an asymmetric shape with respect to the vertical line through the maximum of the rim. The width to the right of this line is 3/2 times the width to the left of this line. (By courtesy of Karin Jacobs, Saarland University)

To explain this we recall first that due to the small height of the dewetting film the magnitude of the slip length is not only comparable to, but it is many times larger than the film thickness. If the rim or other structures have grown to much larger sizes the relative size of the slip length will decrease. In our mathematical model we non-dimensionalized the slip length with the height of the film. Hence we can expect that as the rim grows we may pass from one slip regime to another.

We can demonstrate this behaviour and their corresponding rim shapes also by solving the one dimensional strong-slip equation numerically for long periods of time, ne-

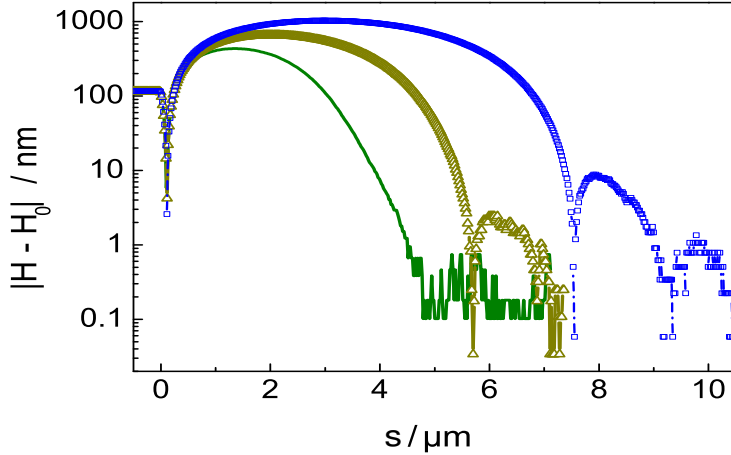


Figure 6: The same rims as in figure 5 for $t = 2900$, $t = 12053$ and $t = 37703$ shown here in a semi-log plot of $|H - H_0|$ to emphasize the transition from monotone to oscillatory decay of the rim tails, where H_0 denotes the unperturbed film thickness. (By courtesy of Karin Jacobs, Saarland University)

glecting inertial contributions. For every value of the slip-length parameter β , the position of the contact-line eventually approaches the power-law behaviour $s(t) \sim t^{2/3}$ that we also obtained numerically and asymptotically in the intermediate slip case (figure 7(a)). Also, the spatial decay of the rim changes from monotonic to oscillatory (figure 7(b)).

In particular for very large values of β , however, $s(t)$ tends to a nearly linear behaviour first before the exponent as determined in figure 7(a) decreases again. This suggests at least that the evolution of the rim passes through several time regimes before eventually following the dynamics of the intermediate slip case. The different regimes were identified and analyzed asymptotically by Evans et al. in the limit of large β . The results published in [47] confirm that in the first long-time regime $1 \ll t \ll \beta^{1/2} / \log^{1/2} \beta$, the contact line position $s(t) \sim t / \log^{1/2} t$, i.e. the dewetting rate is nearly constant. A follow-up publication covering the later stages up to where $s(t)$ follows the $t^{2/3}$ power-law behaviour is in preparation.

4 Stability analysis

In this section we argue that the tendency of the rim instability to develop preferably on the side facing the dewetted area is captured by the intermediate slip model. It has been argued already in [14, 48] that the dependence of the dewetting rate on the rim size in the intermediate slip regime is also responsible for the asymmetric growth of the instability. If one imagines a perturbation that creates thicker and thinner regions in the dewetting rims, then this perturbation will be amplified, and in fact be amplified asymmetrically, since thicker regions will dewet more slowly than the thinner

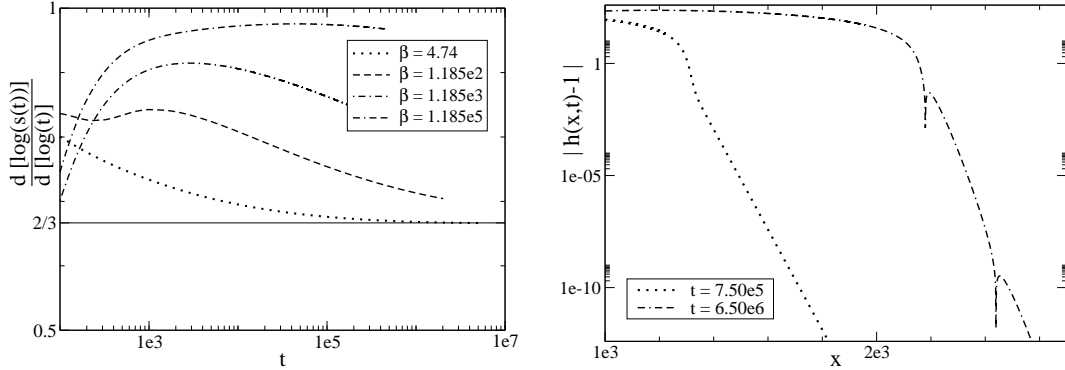


Figure 7: (a) A log-log plot of the evolution of $s(t)$ for the strong slip model with different slip lengths β , using the intermolecular potential (2.16) with $\varepsilon = 0.04$. The bottom thin dotted line is proportional to $t^{2/3}$ to guide the eye. (b) We show the profiles for $\beta = 118.5e-3$ and $\varepsilon = 0.02$ at two different times, in a semilog of $|h(x, t) - 1|$.

ones and will be left behind, leading to finger-type protrusions on dewetted side of the rim. This mechanism is not present for the other regimes where the dewetting rate is largely independent of the rim size. We revisit our earlier results on the linear stability analysis for the no-slip and the intermediate slip regime. Then we show how these results carry over into the nonlinear regime. Finally, we predict the dominant wavelength of the instability in the intermediate slip case.

4.1 Linear theory

For the theoretical description of the rim instability we use linear stability analysis and consider the evolution of a small perturbation of the base state $h_b(x, t)$. Specifically, we introduce the perturbation

$$h(x, y, t) = h_b(x, t) + \delta h_p(x, t) \exp(iky)$$

into the thin film model, with $\delta \ll 1$ and retain only linear terms in δ . Note that while the above ansatz is for a sinusoidal perturbation with a fixed but arbitrary wavenumber k , a general perturbation can be obtained via the superposition principle for the linearized problem using a range of wavenumbers (i.e. via Fouriertransform). Such a general perturbation needs to be considered when discuss in section 4.3 the subtle issue of how the dominant wavenumber is selected for this instability with a time-dependent base state. Experiments by Jacobs et al. [40] and also by Gabriele et al. [49] suggest that the wavelength of the finger pattern increases in time keeping a fixed ratio with the growing width of the rim. We obtain for the linearized equation

$$\frac{\partial h_p}{\partial t} + \mathcal{L}h_p - k^2 \left[(h_b^n h_{px})_x + h_b^n (h_{pxx} - \varepsilon^{-2} \Phi''(h_b/\varepsilon) h_p) \right] + k^4 h_b^n h_p = 0, \quad (4.1)$$

where

$$\begin{aligned} \mathcal{L}h_p &\equiv \frac{\partial}{\partial x} [nh_b^{n-1} (h_{bx} - \varepsilon^{-2} \Phi''(h_b/\varepsilon) h_{bx}) h_p - h_b^n \varepsilon^{-2} \Phi''(h_b/\varepsilon) h_{bx} h_p \\ &\quad + h_b^n (h_{pxx} - \varepsilon^{-2} \Phi''(h_b/\varepsilon) h_{px})] \end{aligned} \quad (4.2)$$

for the no-slip model $n = 3$ and for the intermediate-slip model $n = 2$.

The main challenge in this stability problem is the time dependent base state. This leads to coefficients of the spatial derivatives of h_p in the linearized PDE that are not time independent. Therefore, solutions for the linearized problem cannot be obtained by separation of variables i.e. a classical normal modes approach. Instead, we solve an initial value problem for (4.1), (4.2) for a fixed set of wavenumbers numerically, in tandem with the equation for the base state, and observe how the perturbations evolve in time.

The evolution is computed for a time interval $[t_0, t_1]$ where t_0 and t_1 are the times where the unperturbed front, more specifically, the left contact line regions, estimated for the purpose of this subsection by the position of the turning point, has reached a certain position.

An initial perturbation $h(t)$ is introduced at time t_0 using

$$h_p(x, t_0) = \frac{\partial h_b}{\partial x}(x, t_0), \quad (4.3)$$

which corresponds to a ‘zig-zag’ perturbation, i.e. we perturb both sides of the ridge in the same direction [50].

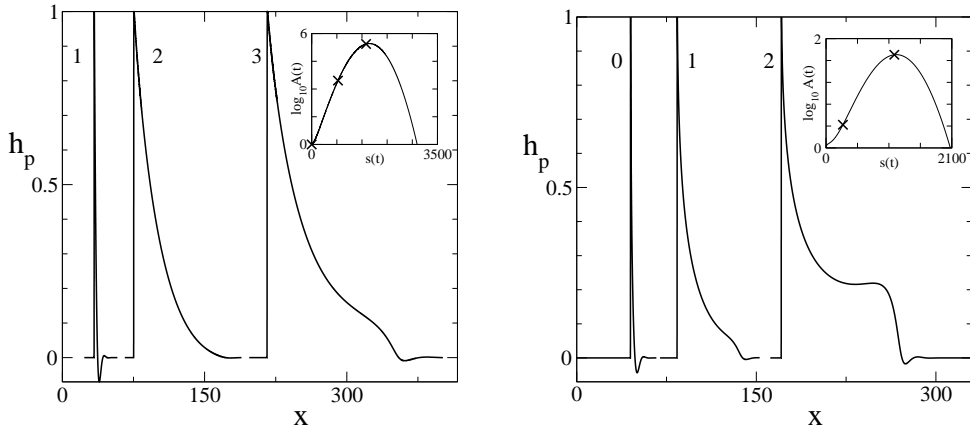


Figure 8: The perturbation profile for wavelength $l = 264.7$ for the intermediate-slip model (left) and the no-slip model (right), at different stages of its evolution, normalized and shifted along the x -axis for better comparison. The labels 1, 2, 3 correspond to the crosses in the inset, which indicate the position $s(t)$ of the base state and the amplification $A(t)$ achieved by $h_p(x, t)$.

To describe the growth of bumps and eventually fingers in the rims, we use the ampli-

fication $A(t)$ of the perturbation with respect to the initial data,

$$A(t) \equiv \frac{\max_x |h_p(x, t)|}{\max_x |h_p(x, t_0)|} \quad \text{for } t_0 \leq t \leq t_1. \quad (4.4)$$

For each fixed wavelength, the perturbation grows as the dewetting proceeds, then it reaches a maximum, after which it decays. Longer wavelengths achieve the maximal amplification factor

$$A_{\max} \equiv \max_{t \geq t_0} A(t)$$

at later stages of the dewetting, when the front has advanced further into the film and the ridge of the base state has grown in size, suggesting that the most amplified wavelength correlates with the width of the ridge [25]. As was shown in [26] the amplification factor grows much faster for the intermediate-slip model compared to the no-slip case. But more significant is the comparison of the shape of the amplified perturbation h_p .

Figure 8 shows profiles of the perturbation h_b for a fixed choice of $k = 0.0237$ at different stages of amplification. For the intermediate-slip case, the initial perturbation (given by (4.3)), has one pronounced maximum and a minimum and slowly evolves into a new profile where the minimum is replaced by a relatively flat part even after the maximum amplification has been achieved. This is in contrast to the no-slip case, where a second bump is created, suggesting a more symmetric shape of the evolving instability.

4.2 Nonlinear dynamics

Our numerical simulations of the full nonlinear no-slip and intermediate-slip models show that small perturbations lead to a visible formation of fingers or bulges once the nonlinearities become important. In addition, the symmetric/asymmetric shapes predicted by linear stability analysis for the no-slip/intermediate-slip case persists upon entry into the nonlinear regime.

To show this we solve the full non-linear two-dimensional problem together with a perturbed base state as initial data, with a monochromatic perturbation, $h(x, y, t_0) = h_b(x, t) + \delta h_p(x, t_0) \cos(qy)$ and $h_p(x, t_0) = \partial_x h_b(x, t_0)$. The numerical method used here is an extension of an ADI-code for higher order PDE [51, 52]. In the y -direction periodic boundary conditions were used and sufficiently large x -domains so that the film profile achieved its far-field values ε and 1. For the intermediate-slip case we see an amplification of the perturbation that eventually leads to fingers (figure 9). Moreover, we observe that the back side of the rim, i.e. the side facing the thick film coating the wafer, is fairly flat, despite the prominent ‘fingers’ that have formed at the dewetting front, and the saddle point and maximum (S and M) are shifted along the x -axis. The plots shown here correspond to an amplification of 480 of the initial perturbation.

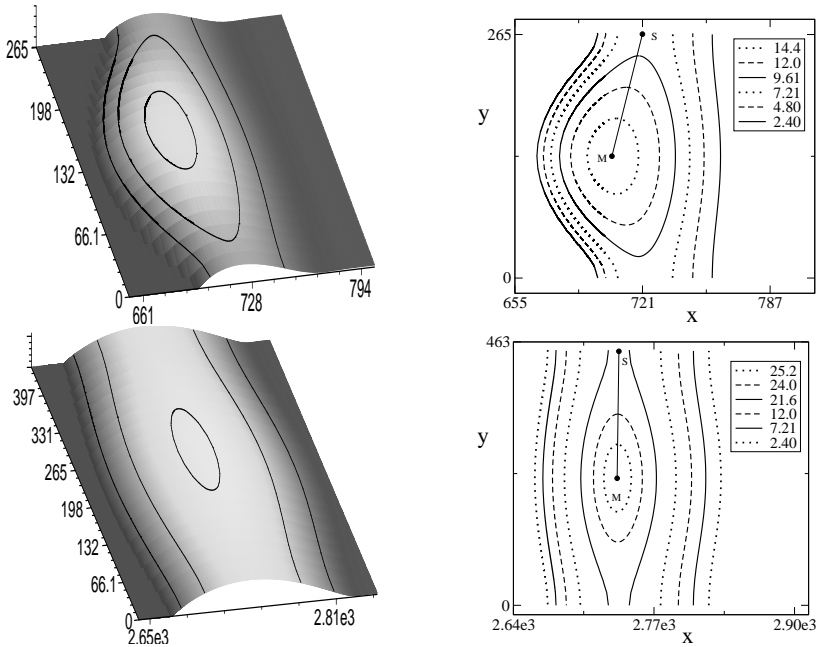


Figure 9: Top: Surface plot and contour lines for $h(x, y, t)$ for the slip case at time $t = 93 \times 10^3$ (corresponding to $s(t) = 685$) and perturbation wavelength $l = 265$. M and S denote the location of the maxima and the saddle point, respectively. Bottom: Surface plot and contour lines for $h(x, y, t)$ for the no-slip case at time $t = 104 \times 10^3$ (corresponding to $s(t) = 2.68 \times 10^3$) and perturbation wave length $l = 446$. M and S denote the location of the maxima and the saddle point, respectively.

In the no-slip case, the amplification achieved for the same wavelengths was much smaller, in fact quite close to the one obtained for linear theory of about 50. The surface plot of the rim appears to be practically unchanged. We therefore include here a surface plot and contour lines for a longer wavelength. For this wavelength, a higher amplification of about 600 is achieved but only at a fairly late stage, where the base state has also become rather large. Hence, the net effect of the corrugation on the ridge still appears to be smaller than in the slip case. Moreover, the contour plots show that the undulations are symmetric. Also the line connecting the saddle point and the maximum (S and M) is very much aligned with the y -direction.

We conclude that the ridge tends to develop a sequence of thinner and thicker parts like in the varicose mode for static rim destabilisation, rather than forming pronounced fingers that protrude into the dewetted area; this is in accordance with our results for the linear theory.

4.3 Wavelength for the intermediate-slip model

So far, we have used numerical simulations of the linearized intermediate slip lubrication model to investigate the stability or instability of perturbations with a fixed wavenumber k . It would be desirable to make quantitative statements that involve

perturbations of arbitrary wavenumber and of arbitrary superposition of such perturbations. In particular, we would like to determine the dominant wavenumber that determines the distance between the bulges (or the troughs) seen in an experiment.

In situations where the base state is stationary, the answer is usually obtained from the mode that has the largest growth rate. A solution to the linearized problems may initially be a superposition of different modes, but since the evolution of each mode is exponentially fast with different growth/decay rates, it will quickly converge to the mode with the largest growth rate. This mode in turn can be found by solving an eigenvalue problem and by maximizing the growth rate over the range of wavenumbers.

In the current problem, we have seen that the growth rate for a fixed wavenumber k is not constant and in fact, perturbations decay after reaching a maximum amplification. Thus, at any given time, we need to find the mode with the largest momentary amplification. Our current numerical setup, however, only allows us to track the evolution for a set of fixed wavenumbers k . Identifying the dominant wavenumber would therefore require us to monitor a large set of wavenumbers and determine the one with the largest amplification at every time t . This seems to be a rather tedious process so we have used an asymptotic approach instead [53].

In the previous section on the shapes of rims, we have seen that for large times, the film profile for the intermediate slip model splits into three asymptotic regions: Two inner solutions near the unperturbed and the residual films, and an outer region which comprises the rim. The leading order outer solution is essentially a traveling wave, given by (3.9)-(3.11). It is a good approximation of the rim once this is large compared to the film thickness in the inner region. Traveling waves have the advantage that they are stationary in a comoving frame of reference, so the stability analysis results in a linear PDE that can be solved by normal modes / eigenvalue analysis. The asymptotic approach can be generalized to the lubrication model for the three-dimensional situation including the spanwise coordinate. It results in a sharp interface model for which the previously found traveling wave is a lower-dimensional solution. We introduce a normal-modes perturbation of the base state

$$h(x, y, t) = h_{\text{tw}}(x - s(t)) + \delta h_1(x - s(t)) \exp(\alpha t + iky), \quad \delta \ll 1,$$

(similarly for the sharp interfaces that bound the outer solution – details in [53]) and find the $O(\delta)$ problem

$$-\sigma \varphi_1 = \left(\varphi^2 (\varphi_{1\xi\xi} - q^2 \varphi_1) \right)_\xi - q^2 \varphi^2 (\varphi_{1\xi\xi} - q^2 \varphi_1) + \varphi_{1\xi}, \quad (4.5)$$

$$\varphi_{1\xi} = \varphi_{\xi\xi} \varphi_1, \quad \varphi^2 \varphi_{1\xi\xi\xi} - \varphi_1 = 0, \quad \text{at } \xi = 0; \quad (4.6)$$

$$\varphi_1 \sim (1/2 - \xi)^{1/2} \quad \text{as } \xi \rightarrow 1/2. \quad (4.7)$$

Here we have scaled the variables as in (3.11), and introduced rescaled wavenumbers and growth rates

$$q = (\lambda^2/\dot{s})k \quad \text{and} \quad \sigma = (\lambda^2/\dot{s}^2)\alpha, \quad (4.8)$$

respectively, to make the resulting eigenvalue problem parameter-free. The eigenvalue for the fastest growing mode was found numerically and turns out to be real; the resulting dispersion relation $\sigma(q)$ is shown in fig. 10.

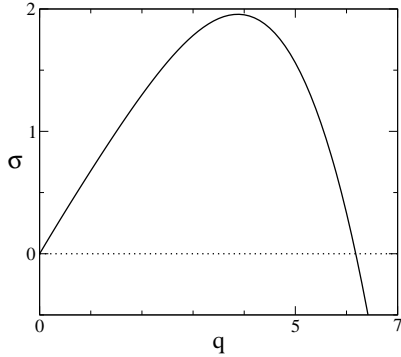


Figure 10: The dispersion relation showing the growth rate σ versus the wavenumber q for the intermediate slip case.

From this dispersion relation, we can obtain the evolution of a single-mode perturbation in the original variables via

$$h_1(x, t) = \frac{\lambda^3}{\dot{s}} \varphi_1(\xi; q) \exp \left[\frac{\dot{s}^2}{\lambda^2} \sigma t \right], \quad \xi = \frac{\dot{s}}{\lambda^2}(x - s), \quad q = \frac{\lambda^2}{\dot{s}} k, \quad (4.9)$$

keeping in mind that we treat the rim as a traveling wave that does not grow in time.

Now, for long times, the rim does grow even if the unperturbed film thickness is small by comparison, and as a result, the speed $\dot{s} \sim t^{-1/3}$ slowly decreases, thus changing the scalings in (4.9). Therefore, the growth rate changes over time. We may still assume that at every given time $t \geq t_0 \gg 1$ (i.e. once the rim is large enough), the evolution of the perturbation is captured for an order one time period by the momentary growth rate $\dot{s}^2 \sigma / \lambda^2$, but to track the evolution and obtain an approximation for the perturbation h_p in the full lubrication model for longer times, we need to accumulate the changes in the growth rate. This suggests using

$$h_p(x, t; k) \sim \varphi_1(\xi; q) \exp \left[\int_{t_0}^t \frac{c(\tau)^2}{\lambda^2} \sigma(q(k; \tau)) d\tau \right], \quad (4.10)$$

as an approximation for $h_p(x, t; k)$, for any fixed k and $t \geq t_0 \gg 1$. Here, ξ and q are given in terms of x and k as in (4.9), $\varphi_1(\xi; q)$ is the normalized eigenfunction corresponding to the eigenvalue $\sigma(q)$, and $c \equiv \dot{s}$.

We can check the approximation (4.10) by comparing the numerical results for the full lubrication and the sharp interface model. First, we look at the perturbation profiles and compare $h_p(x, t; k) / \max_x |h_p(x, t; k)|$ from the full model with $\varphi_1(\xi; q)$. The comparison is done for a fixed wavenumber k at the time t when the amplification factor $A(t) = A(t; k)$ as defined in (4.4) is maximal. Thus, the corresponding q is the cut-off wave number $q_c > 0$ where $\sigma(q_c) = 0$. Fig. 11(a) clearly shows good agreement between the outer region of the full model and the sharp interface result.

To check the time dependent factor in (4.10), we take the maximum with respect to x (and ξ) of the modulus on both sides, and then solve for σ . Recalling the definition of

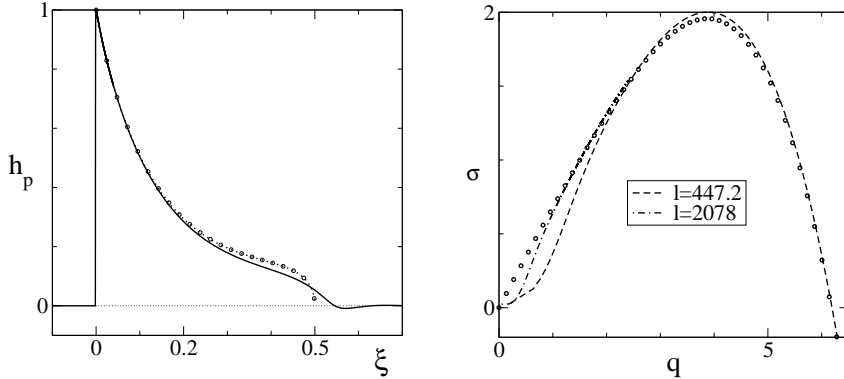


Figure 11: (a) Comparison of the rescaled perturbation $h_p(x, t)$ labelled '3' (solid line) with the eigenfunction of the sharp interface model for the corresponding wavenumber q (circles). (b) Comparison of the rescaled growth rates $\hat{\sigma}$ and wavenumbers q obtained from the solutions h_p for several choices of fixed $l = 2\pi/k$, with the dispersion relation for the sharp interface model (circles). Further explanations for (a) and (b) are given in the text.

the amplification factor in (4.4) we obtain that for fixed k and $t \gg 1$,

$$\sigma(q) \sim \frac{\lambda^2}{c^2} \frac{d}{dt} \ln A(t; k). \quad (4.11)$$

In fig. 11(b), we have plotted both sides of this relation for two different choices for k . The agreement is good except in the range of smaller q . This is not surprising, since small q correspond to smaller t in the full model (recalling that k is fixed) where the condition of validity for a long time (large rim) asymptotic approximation is less satisfied.

We now use (4.10) to investigate the evolution of a more general perturbation a superposition of modes with different wavenumbers. Specifically, we assume the rim is perturbed at a time t_0 and the initial perturbation is given by

$$h_p(x; t_0) = \int_{-\infty}^{\infty} \varphi_1(\xi; k) e^{iky} dk. \quad (4.12)$$

Note that due to our normalisation of φ_1 this implicitly assumes that the initial amplitude at $t = t_0$ of each contribution is one for all wavenumbers. By applying (4.10) the perturbation at time $t \gg t_0 \gg 1$ is found to be

$$h_p(x; t) = \int_{-\infty}^{\infty} \exp \left[\int_{t_0}^t \frac{c(\tau)^2}{\lambda^2} \sigma(q(k; \tau)) d\tau \right] \varphi_1(\xi; k) e^{iky} dk. \quad (4.13)$$

At any given time, the dominant wave number k_d is the one for which the amplification i.e. the square bracket is maximal. Taking derivatives with respect to k we obtain

$$\int_{t_0}^t c(\tau) \sigma' \left(\frac{\lambda^2}{c(\tau)} k_d \right) d\tau = 0. \quad (4.14)$$

Since $1/c(\tau)$ is monotonically increasing, we can use $Q = k_d \lambda^2 / c(\tau)$ as integration variable. Substituting this in and recalling $c(\tau) \sim \tau^{-1/3}$ for all $\tau \geq t_0 \gg 1$ yields

$$0 = \int_{q(k_d; t_0)}^{q(k_d; t)} \frac{-c^3}{\lambda^2 k_d c_\tau} \sigma'(Q) dQ \sim \int_{q(k_d; t_0)}^{q(k_d; t)} Q \sigma'(Q) dQ \quad (4.15)$$

for $t \gg t_0 \gg 1$. Since $q(k_d; t_0) = q(k_d; t)c(t)/c(t_0) \rightarrow 0$ for $t \gg t_0$, we can replace the lower integration limit by 0. Integration by parts then leads us to an “equal area” condition

$$\int_0^{q(k_d; t)} (\sigma(Q) - \sigma(q(k_d; t))) dQ = 0. \quad (4.16)$$

The function $\sigma(Q)$ is the dispersion relation for the sharp interface model that was previously obtained from numerical calculations. Solving for $q_d \equiv q(k_d; t)$ we numerically obtain $q(k_d; t) = 5.3$, from which we can obtain the dominant wave-number in the scaling of the full lubrication via $k_d = q_d c(\tau) / \lambda^2$. The width of the rim is $w(t) = (1/2)(\lambda^2 / c)$, thus $k_d w(t) = q_d / 2$, which results in

$$\frac{l_d}{w(t)} = \frac{2\pi}{q_d / 2} \approx 2.4 \quad (4.17)$$

for the dominant wavelength $l_d = 2\pi/k_d$. This implies in particular that the dominant wavelength grows with the same scaling as the width of the rim. Also note that the result is different from the preferred and the cut-off wavelength, $l_m = 3.24$ and $l_c = 2.03$, respectively. These are obtained upon using q_m (where σ is maximal) and $q_c > 0$ (where σ is zero) in (4.17) instead of q_d .

5 Conclusion

In this paper we have presented our analysis on the morphology and stability of a rim that is formed at front of a dewetting polymer film. By revisiting some of our previous work together with our new results, our goal was to give a coherent theory that can explain the dewetting patterns observed in experiments for the model system PS on a hydrophobically coated silicon/silicon oxide wafer. The aim of this fundamental study is to be able to eventually simply infer material properties, such as the interfacial conditions for polymer/substrate system, by extracting information on the morphological signatures of the evolving patterns.

We believe that on the basis of this theory it is now possible to infer the magnitude of the effective slippage at the polymer/coating interface by observing in an experiment the cross sectional rim shape, the symmetric/asymmetric shapes of the evolving instability, as well as the time scales on which these occur.

The model system used in the experiments considers polymers below the entanglement length at very slow flow conditions and so the governing hydrodynamic equations for bulk of the liquid were taken to be the Navier-Stokes equations. In fact the

dewetting dynamics were so slow that inertial terms are negligible. The only remaining feature of non-Newtonian behaviour is the magnitude of slippage, that plays a dominant role, also because of the small scale of the thickness of the liquid polymer film.

For liquid polymer above entanglement length however, other properties, such as elastic effects shall also be taken into account. At this point we only have developed appropriate thin film models for Jeffreys-type viscoelastic models. However, we have not explored their properties in the same detail as for the Newtonian case. Developing this theory further and seeking experimental validation for it is part of ongoing research.

Acknowledgement

The authors thank Karin Jacobs, Renate Fetzer, Oliver Bäumchen, Ludovic Marquant, Ralf Blossey, Peter L. Evans, John R. King, Markus Rauscher and Thomas P. Witelski for the many fruitful discussions and collaborations.

The authors are very grateful for the support by the DFG Priority Programm 1164 “Nano- and Microfluidics” and MATHEON.

References

References

- [1] H. Huppert. Flow and instability of a viscous current down a slope. *Nature*, 300:427–429, 1982.
- [2] N. Silvi and E.B. Dussan V. On the rewetting of an inclined solid surface by a liquid. *Physics of Fluids*, 28:5–7, 1985.
- [3] A. L. Bertozzi and M. P. Brenner. Linear stability and transient growth in driven contact lines. *Phys. Fluids*, 9(3):530–539, March 1997.
- [4] S. M. Troian, E. Herbolzheimer, S. A. Safran, and J. F. Joanny. Fingering instabilities of driven spreading films. *Europhys. Lett.*, 10:25–30, 1989.
- [5] A. M. Cazabat, F. Heslot, S. M. Troian, and P. Carles. Finger instability of thin spreading films driven by temperature gradients. *Nature*, 346(6287):824–826, August 1990.
- [6] J. B. Brzoska, F. Brochard-Wyart, and F.B. Rondelez. Exponential growth of fingering instabilities of spreading films under horizontal thermal gradients. *Europhysics Letters*, 19:97–102, 1992.

- [7] Dawn E. Kataoka and Sandra M. Troian. A theoretical study of instabilities at the advancing front of thermally driven coating films. *J. Coll. Int. Sci.*, 192:350–362, 1997.
- [8] A. L. Bertozzi, A. Münch, X. Fanton, and A. M. Cazabat. Contact line stability and ‘undercompressive shocks’ in driven thin film flow. *Phys. Rev. Lett.*, 81(23):5169–5172, December 1998.
- [9] P. Gilberto López, S. George Bankoff, and Michael J. Miksis. Non-isothermal spreading of a thin liquid film on an inclined plane. *J. Fluid. Mech.*, 11:1–39, 1996.
- [10] A. Münch and B. A. Wagner. Numerical and asymptotic results on the linear stability of a thin film spreading down a slope of small inclination. *E.J.A.M.*, 10:297–318, 1999.
- [11] K. Jacobs, S. Herminghaus, and K. R. Mecke. Thin liquid polymer films rupture via defects. *Langmuir*, 14:965–969, 1998.
- [12] F. Brochard-Wyart, G. Debregeas, R. Fondecave, and P. Martin. Dewetting of supported viscoelastic polymer films: Birth of rims. *Macrom.*, 30:1211, 1997.
- [13] C. Redon, F. Brochard-Wyart, and F. Rondelez. Dynamics of dewetting. *Phys. Rev. Lett.*, 66(6):715–718, 1991.
- [14] C. Redon, J. B. Brzoska, and F. Brochard-Wyart. Dewetting and slippage of microscopic polymer films. *Macromolecules*, 27:468–471, 1994.
- [15] R. Fetzer, K. Jacobs, A. Münch, B. Wagner, and T. P. Witelski. New slip regimes and the shape of dewetting thin liquid films. *Phys. Rev. Lett.*, 95:127801, 2005.
- [16] F. Rayleigh. On the instability of jets. *Proc. London Math. Soc.*, 1:1–10, 1878.
- [17] J. Plateau. Experimental and theoretic steady state of liquids subjected to nothing but molecular forces, 1873.
- [18] G. Reiter. Dewetting of thin polymer films. *Phys. Rev. Lett.*, 68(1):75–78, 1992.
- [19] G. Reiter, A. Sharma, A. Casoli, M.-O. David, R. Khanna, and P. Auroy. Thin film instability induced by long-range forces. *Langmuir*, 15:2551–2558, 1999.
- [20] A. Sharma and R. Khanna. Pattern formation in unstable thin liquid films. *Phys. Rev. Lett.*, 81(16):3463–3466, 1998.
- [21] A. Sharma and R. Khanna. Pattern formation in unstable thin liquid films under influence of antagonistic short- and long-range forces. *Journal of Chemical Physics*, 110(10):4929–4936, 1999.
- [22] R. Xie, A. Karim, J. F. Douglas, C. C. Han, and R. A. Weiss. Spinodal dewetting of thin polymer films. *Phys. Rev. Lett.*, 81:1251–1254, 1998.

- [23] C. Neto and K. Jacobs. Dynamics of hole growth in dewetting polystyrene films. *Physica A*, 339:66–71, 2004.
- [24] A. Sharma and G. Reiter. Instability of thin polymer films on coated substrates: Rupture, dewetting and drop formation. *J. Coll. Int. Sci.*, 178:383–389, 1996.
- [25] J.-L. Masson, O. Olufokunbi, and P. F. Green. Flow instabilities in entangled polymer films. *Macromolecules*, 35:6992–6996, 2002.
- [26] A. Münch and B. Wagner. Contact-line instability of dewetting thin films. *Physica D*, 209:178–190, 2005.
- [27] A. Münch, B. Wagner, and T. P. Witelski. Lubrication models with small to large slip lengths. *Journal of Engineering Mathematics*, 53(3-4):359–383, 2006.
- [28] K. Jacobs, R. Seemann, G. Schatz, and S. Herminghaus. Growth of holes in liquid films with partial slippage. *Langmuir*, 14:4961–4963, 1998.
- [29] L. Bocquet and J. L. Barrat. Flow boundary conditions from nano- to micro-scales. *Soft Matter*, 3:685–693, 2007.
- [30] C. Neto, D. R. Evans, E. Bonaccurso, H.-J. Butt, and V. S. J. Craig. Boundary slip in newtonian liquids: a review of experimental studies. *Rep. Prog. Phys.*, 68:2859–2897, 2005.
- [31] S. Gabriele, S. Coppée, G. Reiter, and P. Damman. On the mechanics of rim instabilities in viscoelastic polymer thin films. *Eur. Phys. J. Special Topics*, 166:55–61, 2009.
- [32] F. Brochard-Wyart, P.-G. de Gennes, H. Hervet, and C. Redon. Wetting and slippage of polymer melts on semi-ideal surfaces. *Langmuir*, 10:1566–1572, 1994.
- [33] G. Reiter and A. Sharma. Auto-optimization of dewetting rates by rim instabilities in slipping polymer films. *Phys. Rev. Lett.*, 80:166103, 2001.
- [34] R. Konnur, K. Kargupta, and A. Sharma. Instability and morphology of thin liquid films on chemically heterogeneous substrates. *Phys. Rev. Lett.*, 84:931–934, 2000.
- [35] R. Fetzer, A. Münch, B. Wagner, M. Rauscher, and K. Jacobs. Quantifying hydrodynamic slip: A comprehensive analysis of dewetting profiles. *Langmuir*, 23:10559–10566, 2007.
- [36] R. Blossey, A. Münch, M. Rauscher, and B. Wagner. Slip vs viscoelasticity in dewetting thin films. *European Physical Journal E - Soft Matter*, 20:267–271, 2006.

- [37] M. Rauscher, A. Münch, B. Wagner, and R. Blossey. A thin-film equation for viscoelastic liquids of jeffreys type. *European Physical Journal E - Soft Matter*, 17:373–379, 2005.
- [38] R. Fetzer and K. Jacobs. Slippage of newtonian liquids: Influence on the dynamics of dewetting thin films. *Langmuir*, 23:11617–11622, 2007.
- [39] O. Bäumchen and K. Jacobs. Slip effects in polymer thin films. *J. Phys. Condens. Matter*, 22:033102, 2010.
- [40] L. Marquant, O. Bäumchen, and K. Jacobs. private communication, 2010.
- [41] R. Seemann, S. Herminghaus, and K. Jacobs. Gaining control of pattern formation of dewetting films. *J. Phys. Condens. Matter*, 13:4925–38, 2001.
- [42] K. Jacobs, R. Seemann, and S. Herminghaus. Stability and dewetting of thin liquid films, 2008. in: Polymer thin films, ed. O.K.C. Tsui and T.P. Russell, Singapur: World Scientific.
- [43] F. Brochard and P.-G. de Gennes. Shear-dependent slippage at a polymer/solid interface. *Langmuir*, 8:3033–3037, 1992.
- [44] J. L. Goveas and G. H. Fredrickson. Apparent slip at a polymer-polymer interface. *Eur. Phys. J. B*, 2:79–92, 1998.
- [45] J. C. Flitton and J. R. King. Surface-tension-driven dewetting of Newtonian and power-law fluids. *J. Engr. Math.*, 50:241–266, 2005.
- [46] Stefanella Boatto, Leo P. Kadanoff, and Piero Olla. Traveling-wave solutions to thin-film equations. *Physical Review E*, 48(6):4423–4431, 1993.
- [47] P. L. Evans, J. R. King, and A. Münch. Intermediate-asymptotic structure of a dewetting rim with strong slip. *Applied Mathematics Research eXpress*, 2006:1–25, 2006.
- [48] G. Reiter and R. Khanna. Kinetics of autophobic dewetting of polymer films. *Langmuir*, 16:6351–6357, 2000.
- [49] S. Gabriele, S. Sclavons, G. Reiter, and P. Damman. Disentanglement time of polymers determines the onset of rim instabilities in dewetting. *Phys. Rev. Lett.*, 96:156105, 2006.
- [50] F. Brochard-Wyart and C. Redon. Dynamics of liquid rim instabilities. *Langmuir*, 8:2324–2329, 1992.
- [51] A. Münch. Fingering instability in dewetting films induced by slippage, 2004.
- [52] T.P. Witelski and M. Bowen. Adi schemes for fourth-order nonlinear diffusion equations. *Appl. Num. Math.*, 45:331–353, 2003.
- [53] J. King, A. Münch, and B. Wagner. Linear stability analysis of a sharp-interface model for dewetting thin films. *J. Engrg. Math.*, 63:177–195, 2009.